

## TEMPERATURE STRUCTURE IN ABELL 1367

R. HANK DONNELLY, M. MARKEVITCH, W. FORMAN, C. JONES, L. P. DAVID

Harvard-Smithsonian Center for Astrophysics, 60 Garden street, Cambridge, MA 02138, USA

and

E. CHURAZOV, AND M. GILFANOV

Max Planck Institute für Astrophysik, Karl-Schwarzschild-Strasse 1, 85740 Garching bei München, Germany

and

Space Research Institute (IKI), Profsouznaya 84/32, Moscow 117810, Russia

*accepted by The Astrophysical Journal*

### ABSTRACT

We study the temperature structure of the rich cluster of galaxies Abell 1367 using two independent methods of correcting for the ASCA PSF. The results of the two methods are in excellent agreement and give solid evidence of a strong and localized shock in the intracluster medium (ICM). Our analysis suggests that we are observing the merger of two subclusters. We find that the lower luminosity subcluster, located to the northwest, has a higher temperature of  $4.2 \pm 0.3$  keV, compared to the more luminous southeast subcluster, whose temperature is  $3.2 \pm 0.1$  keV. An analysis of the ROSAT surface brightness profiles of both subclusters is also presented. The data agree well with predictions from numerical simulations of mergers between subcluster sized masses, in particular, with early stages of the merger, prior to the first core passage.

*Subject headings:* galaxies: clusters: individual (A1367) — intergalactic medium — X-rays: galaxies — methods: data analysis

### 1. INTRODUCTION

Optical and X-ray studies (e.g. Geller & Beers 1982; Forman et al. 1981; Dressler & Shectman 1988; Jones & Forman 1992; Mohr et al. 1994; Bird 1994; Slezak et al. 1994) have shown that galaxy clusters are dynamically evolving systems exhibiting a variety of substructure. Thus, we expect to see key identifiers of the merging process in the temperature maps of galaxy clusters with significant substructure. In particular, in the early stages of an unequal merger, i.e. one subcluster larger than the other, simulations show significant heating of the smaller subcluster above the temperature of the local ICM (Evrard 1990a and b; Schindler & Müller 1993) as well as the development of a shock located between the two subclusters.

Abell 1367 has previously been identified as having significant optical and X-ray substructure (Bechtold et al. 1983; Grebenev et al. 1995). The X-ray emission is elongated along a southeast-northwest axis, and contains small, localized “clumps”. The cluster has a relatively cool gas temperature and a high spiral fraction (see Bahcall 1977 and Forman & Jones 1982) typical of what is expected for a dynamically young system.

In this paper we report on the analysis of the structure of the A1367 galaxy cluster as mapped by the X-ray emission observed with the ROSAT PSPC and the ASCA detectors. In Section 2, we apply two independent methods which account for the energy dependent ASCA Point-Spread-Function(PSF) and produce moderate spatial resolution ( $\sim 4'$ ) temperature maps. This is an extension of the work presented by Churazov et al. (1996a). We also describe our surface brightness analysis of the ROSAT PSPC data. Section 3 presents the results of the temperature determinations and our estimates of the masses of each subcluster. Finally, Section 4 briefly summarizes our

results. All distance dependent quantities have assumed  $H_0 = 50 \text{ km s}^{-1} \text{ Mpc}^{-1}$ ,  $q_0 = 0.5$ , all coordinates are given in the J2000 system, and unless otherwise noted all error bars are 67% confidence level ( $1\sigma$ ) errors.

### 2. OBSERVATIONS & METHODS

#### 2.1. ROSAT Analysis

The ROSAT PSPC observed A1367 from 29 November to 2 December 1991 (RP800153); observing details are listed in Table 1. We corrected the PSPC image for telescope vignetting as well as the removal of times with high solar/particle backgrounds using the standard procedures outlined by Snowden (1994; also Snowden et al. 1994). By combining only the data from Snowden bands 4 through 7 (0.44-2.04 keV), we excluded the lower energies, which are likely to have higher background X-ray contamination. The background was not subtracted during this stage of the processing; instead, it was included as a constant component in our fits of the surface brightness, as described below. The central area of the PSPC image is shown in Figure 1, after having been smoothed with a  $30''$  Gaussian.

The extended cluster emission appears peaked in two locations, a primary peak near  $11^h 44.8^m +19^\circ 42'$  (hereafter the SE subcluster) and a secondary peak towards the northwest at  $11^h 44.4^m +19^\circ 52'$  (hereafter the NW subcluster). The temperature distribution and previous radio results— both discussed later in this paper— suggest that we are observing the merger of two subclusters. Because of this, we performed a surface brightness analysis deriving the X-ray surface brightness profile and the core radius assuming a standard  $\beta$ -model on each region independent of and excluding the other. This data also were used as a surface brightness model for one of the spectroscopic analyses of the ASCA data (Method B).

To aid in the location of potential point sources contaminating the field, we smoothed the PSPC image on scales from  $30''$  to  $8'$ . The smaller scales were used to locate point sources near the center of the image, while the larger scales were used near the edges where the distortions of the PSF are large. Potential point sources were identified by eye and these areas were excluded from further analysis of the surface brightness distribution.

To accurately locate the peaks of the two subclusters, we masked off one peak as well as the point sources, and centred the other. We then repeated the process for the other peak. The equatorial coordinates (J2000) of the two peaks in the ROSAT image coordinate frame are: SE-  $\alpha = 11^h 44^m 50^s$   $\delta = 19^\circ 41' 44''$ , NW-  $\alpha = 11^h 44^m 22^s$   $\delta = 19^\circ 52' 27''$ . These appear to be offset  $+0.175^\circ$  in RA and  $+11''$  in Dec from the true sky position based upon the location of NGC 3862 (the bright X-ray point source in the southeast). This is roughly consistent with typical pointing errors for ROSAT.

To generate radial profiles, we defined  $1'$  wide annuli, with inner radii from  $0'$  to  $46'$ , centered on each peak. To avoid contamination of one subcluster by the other, we excluded the third of each annulus which was on the side towards the other subcluster. For the SE subcluster the excluded azimuths ranged from  $255^\circ$  to  $15^\circ$  and for the NW subcluster from  $75^\circ$  to  $195^\circ$  (with the angle measured counter-clockwise from North).

We then measured the average surface brightness ( $\text{cts s}^{-1} \text{arcmin}^{-2}$ ) in each annulus, and fit the resultant surface brightness profiles with a standard hydrostatic, isothermal  $\beta$ -model:

$$\Sigma(r) = \Sigma_0 \left[ 1 + \left( \frac{r}{R_c} \right)^2 \right]^{-(3\beta - \frac{1}{2})} \quad (1)$$

(Cavaliere & Fusco-Femiano 1976). Because of A1367's low redshift ( $z = 0.0215$ ) the cluster emission overfills even the PSPC's large field of view. This makes direct measurement of the background difficult. Therefore, we included a constant background component in our model. The best fit backgrounds were  $(1.79 \pm 0.17) \times 10^{-4}$  and  $(1.29 \pm 0.29) \times 10^{-4} \text{ cts s}^{-1} \text{arcmin}^{-2}$  for the SE and NW subclusters respectively, which are both consistent with typical PSPC backgrounds. While the best fit background for the SE subcluster is slightly larger, possibly indicating a small amount of contamination by the NW subcluster, the errors are consistent with a single constant background. The results of our fitting are given in Table 2 and the fits themselves are shown in Figure 2.

## 2.2. ASCA Analysis

To correctly characterize the temperature from ASCA data at some location for an extended source, we must account for the extended and energy dependent PSF of the telescope (Takahashi et al. 1995). The primary difficulty for spatially resolved spectroscopy is caused by the outer part, or wings, of the PSF. Failing to correct for this component can lead to spurious temperature and abundance gradients, although for A1367, due to its relatively low temperature and large spatial extent, these effects are not expected to be very strong.

We have employed two independent methods which

account for the broad energy dependent ASCA Point-Spread-Function (PSF) to construct temperature maps for A1367. Method A (Churazov et al. 1997; Gilfanov et al. 1997), provides a rapid approximate correction of the extended wings of the PSF. In contrast, Method B (Markovitch et al. 1997) performs an exact convolution of a surface brightness model with the PSF and the effective area of the telescope to generate model spectra which are then compared to the data.

ASCA observed A1367 on 4-5 December 1993, with four pointings, one pair centered on the northwest region and the other centered on the southeast. Within each pair, the two pointings were offset from each other by  $1.89'$  along a roughly SE-NW axis. This offset allowed an evaluation of any systematic effects. Details of the ASCA observations also are given in Table 1.

Preliminary to correcting the PSF, the ASCA data were "cleaned" with standard processing tools (Arnaud 1993). A cutoff rigidity of  $8 \text{ GeV}/c$ , minimum Earth elevation angles of  $5^\circ$  for the GIS and  $20^\circ$  for the SIS, and maximum count rate of  $50 \text{ cts/s}$  in the radiation belt monitor were used. The GIS's background was generated from an appropriately weighted combination of background maps for all rigidities, and for the SIS's, all hot-pixel events were removed and the background maps were scaled by total exposure.

### 2.2.1. Approximate Fitting of the Wings of the ASCA PSF- Method A

Method A approximates the ASCA PSF as having a core and broader wings (see Churazov et al. 1997 and Gilfanov et al. 1997 for details). The core PSF is corrected explicitly while the energy dependant PSF of the wings is corrected using a Monte Carlo algorithm. After the approximate subtraction of the scattered flux in the wings of the PSF, the temperature is determined using one of two approaches. The first fits the spectrum in each  $15''$  pixel with a linear combination of two fiducial single-temperature spectra and then smooths the result to reduce the noise (Churazov et al. 1996b). This approach yields a continuous (unbinned) temperature map of the cluster. Central to this method is the fact that thermal spectra having typical cluster temperatures ( $\gtrsim 2 \text{ keV}$ ) can be approximated as a linear combination of two spectra bounding the temperature range in the cluster (Churazov et al. 1997). For A1367 we used fiducial spectra with  $kT=2$  and  $6 \text{ keV}$ . The results for the GIS data for A1367 are shown in Figure 3, along with intensity contours from the ASCA data. Only temperatures with a  $\frac{T+\sigma_T}{T-\sigma_T} < 1.5$  are shown. Results for the SIS are similar, although with a smaller detector field of view.

The second temperature fitting approach proceeds by defining a series of regions which we chose to lie straddling the line connecting the two subclusters (see Figure 3). Each region was  $5'$  in width and approximately  $16'$  in length. We excluded a region  $5'$  in diameter around the bright point source (NGC 3862) near the SE subcluster, so as to prevent its signal from contaminating our temperature fits. This diameter was chosen to be large enough to more than contain the central part of the PSF. In addition, we estimate that the point source contributes only about 33% of the total flux in this excluded region, which gives us confidence that there is little contamination in the

neighboring regions (#1 and #2). All of the data in each region were binned together, and then output as composite spectra. These spectra were then fit with a standard Raymond-Smith model using the XSPEC package utilizing the data from 1.5-2.0 and 2.5-11.0 keV. These limits were chosen to exclude the poorly calibrated region near the gold edge at 2.2 keV, and the extreme low energies for which the PSF remains poorly determined.

### 2.2.2. Multiple Region Simultaneous Spectral Fitting—Method B

Method B employs a model surface brightness distribution which is convolved with the mirror effective area and the ASCA PSF (Takahashi et al. 1995) to produce model spectra for a set of user defined regions in the ASCA detector planes. The spectra from the desired regions are then fit simultaneously. A more detailed description, including a discussion of systematic uncertainties, can be found in Markevitch et al. (1996 and 1997).

Integral to this method is the use of a detailed surface brightness model. To this end we used the ROSAT PSPC image from our surface brightness analysis, blocked, rotated and shifted to coincide with the ASCA image. We chose the regions used in this analysis to be identical to those defined in Method A.

To perform the actual temperature fitting, the pulse height data were binned in energy to achieve an adequate signal to noise ratio. The same energy range used in Method A was utilized, with the bins defined to be 1.5-2.0, 2.5-3.5, 3.5-5.5 and 5.5-11.0 keV. All of the processing so far was performed independently for each detector (SIS-0, SIS-1, GIS-2, and GIS-3) for each pointing. To determine the temperatures in each of the model regions, all of the SIS data— from both the 0 and 1 detectors— for all four pointings, for all the regions and for all of the energy bands were simultaneously fit. A similar procedure was followed for the GIS.

To estimate the errors in our temperature solutions, we measured the standard deviation of the distribution of fit temperatures from 200 simulated spectra. Each spectrum was constructed by performing a Monte-Carlo simulation of the counts in each energy band, assuming a Gaussian distribution about the observed number of counts in that energy band in the data. The systematic errors were added to the data and model as appropriate.

## 3. RESULTS & DISCUSSION

### 3.1. Temperature Structure

Figure 3 shows the continuous temperature map produced by Method A and indicates a temperature gradient across the cluster, increasing from the 3.0 keV in the SE to 4.3 keV in the NW. The regions defined earlier were designed to assess the significance of this trend, spanning the cluster along an axis from the SE to the NW (see Figure 1 and Figure 3). Both spectral analysis methods (A & B) discussed above were applied to the data and the results of the fitting are given in Table 3 and Figure 4.

The first feature of note in Figure 4 is the excellent agreement between the two methods for both the GIS and SIS detectors. This gives us confidence that the results of our fitting procedure are correct, at least to our knowledge of the ASCA PSF.

The next feature to note in Figure 4 is that the temperature variation appears to be abrupt rather than smooth, with a jump occurring in region #4. The spectral fits for the SE subcluster (regions #1-3) are consistent with a constant temperature of  $3.2 \pm 0.1$  keV, and although the data for the NW subcluster (regions #5-7) have larger error bars, they are consistent with a constant, but higher, temperature of  $4.2 \pm 0.3$  keV, spanning the bulk of the emission.

To study the nature of the transition and as a consistency check, we shifted the regions by one half of a box width (2.5') along the SE-NW axis and reapplied Method A to the GIS data. For the shifted regions that overlapped with the original regions #1–#3, i.e. the SE subcluster, the fit temperatures were unchanged. Similarly the temperatures for the NW subcluster, regions #5–#7, were unchanged. However, the abruptness of the transition from SE to NW became more pronounced.

Focusing on the regions near the transition— #3, #4 and #5— the original GIS Method A temperatures were 3.3, 3.6 and 3.8 keV respectively. After the shift, the region to the southeast of the middle of #4 had a temperature of 3.4 keV while the temperature of the region to the northwest was 3.9 keV.

If the extent of the transition was large, the shifted regions would, by their partial inclusion of intermediate gas in *two* shifted regions, have had a higher temperature than before on the southeastern side and a lower temperature on the northwestern side. Instead the intermediate region effectively disappeared. Region #4 appears to have been intermediate because it contained nearly equal amounts of the SE and NW subclusters.

This abrupt temperature change indicated by the temperature fits with and without the shift is strongly suggestive of a shock located nearly at the midpoint of region #4, that has been generated during a collision between the two galaxy subclusters. In fact the temperature distribution and intensity contours are very similar in nature to cross-sectional temperature and projected surface brightness profiles shown in Figures 3b-c and 5b-c respectively in Schindler & Müller (1993). In these simulations, at 0.95 Gyr after the beginning of the merger, the smaller subcluster shows extensive heating in its core relative to its initial state as well as a strong gradient with radius. By 2.66 Gyr the cores are nearly in contact and the thermal gradient in the smaller subcluster has dissipated considerably. At the same time the temperature of the core of larger member of the merger has begun to increase and develop a thermal gradient.

In A1367, the measured gas temperatures of both the SE and NW subclusters are hotter than that expected from the luminosity-temperature relation for clusters (e.g. Edge & Stewart 1991; David et al. 1993). Although there is moderate dispersion in the  $L_x$ -T relation it is possible that the SE subcluster gas also has begun to be heated due to the merger. This potential heating of the SE subcluster and apparent lack of thermal gradients in both subclusters as well as the clear separation of the two peaks suggests that we are observing the merger at a stage intermediate to those shown in the figures of Schindler & Müller, at approximately 1.8 Gyr after the onset.

Observations by Gavazzi et al. (1995) also suggest that A1367 is currently undergoing a merger. They find three head-tail radio galaxies in the NW subcluster that have

extremely large radio/IR flux ratios as well as an extreme excess of giant HII regions on their leading edges, all of which are pointed towards the SE subcluster. From simulations, Roettiger et al. (1996) find that the expected shock generated from a merger event could “induce a burst of star formation” as well as help to generate head-tail morphology.

Finally, in an effort to generate a detailed map of the cluster we divided each of the rectangular regions into three roughly square ( $5' \times 5'$ ) subregions, and re-applied Method A. By combining the temperature fitting for the GIS and SIS data we attempted to improve the statistics in each region and produce composite temperatures. The results are shown in Figure 5. We also added four regions to the northeast of regions #1-#4 to examine the cool feature that appears in Figure 3. We see a trend of decreasing temperature from west to east across the subregions around the SE subcluster (#41 to #14). This may indicate that the merger is slightly oblique rather than head-on; however, we note that the variations are not highly significant.

Figure 5 also helps to rule out the possibility that we are viewing the NW subcluster through a hot isothermal shell. In that case, we would expect the temperature to decline with decreasing projected radius, which is opposite to the trend found in our temperature maps.

### 3.2. Density Profiles

Typical values of the core radius for relaxed clusters range up to 0.6 Mpc with the peak of the distribution around 0.2 Mpc (Jones & Forman 1984). The core radii of the SE and NW subclusters are 0.42 and 0.49 Mpc respectively, and lie significantly toward the high end of the distribution. Simulations by Roettiger et al. (1996) show that during a merger the core radius of the gas can increase by a factor of two or more due to the increase in the central entropy of the gas through shocks. Further, the core radius of the NW subcluster is larger than that of the SE subcluster indicating that the NW subcluster is even farther from a relaxed state than the SE subcluster.

Similarly, the best fit values of  $\beta$  are 0.73 and 0.66 for the SE and NW respectively, which are relatively large compared to relaxed clusters with temperatures similar to those of A1367. In a relaxed cluster  $\beta$  generally lies in the range of 0.4 to 0.8 and increases with the gas temperature. The typical value for a 4 keV cluster is between 0.5 and 0.6 (Jones & Forman 1997).

### 3.3. Abundances

For Method A, where we fit the spectrum for each region independently, we allowed the abundance to be a free parameter in the fit. The results with error bars are given in Table 3 and in Figure 6. Even though the error bars are quite large, there is some suggestion from these results that the NW subcluster has a lower abundance than the SE subcluster. To test this we defined two regions on the GIS data, one surrounding each subcluster, and again applied Method A. The results from these fits gave abundances relative to solar of  $0.26 \pm 0.06$  and  $0.11 \pm 0.05$  for the SE and NW subclusters respectively. We note, however, that large changes in the abundance, e.g. assuming an abundance of 0.3 solar for the NW subcluster, had no significant effect on the fit temperatures.

In Method B, where the abundances were held fixed during the fits, we determined the temperatures twice, once with an abundance of 0.3 solar and once with an abundance of 0.4 solar. The differences in the temperature solutions were inconsequential. Because the temperatures are relatively insensitive to abundance, for Method B we have presented only the results using the typical abundance of 0.3 solar.

### 3.4. Mass Estimates

We made two estimates for the mass of each subcluster by applying the equation of hydrostatic equilibrium with the same density profiles, but two independent temperatures. In the case of a merger and the subsequent heating of the ICM gas, the mass estimates though very uncertain do provide a means of comparing the masses of the two subclusters. The first estimate uses the temperature we derived from our spectral fitting; the second came from applying the observed relation between temperature and X-ray luminosity found by David et al. (1993). Independent of these calculations we also estimated the masses of the X-ray emitting gas in each subcluster.

The assumption of hydrostatic equilibrium and spherical symmetry gives a simple equation for the total mass of the emitting system which when combined with a density profile given by an isothermal  $\beta$ -model reduces to:

$$M(r) = 1.13 \times 10^{15} \beta \left( \frac{T}{10 \text{ keV}} \right) \left( \frac{r}{\text{Mpc}} \right) \frac{(r/R_c)^2}{1 + (r/R_c)^2} M_{\odot}. \quad (2)$$

To test the assertion of isothermality, we constructed three semi-circular annuli—radii 0-6', 6-12', and 12-18'—centered on each subcluster such that each sampled the region *away* from the other subcluster in order to exclude the region of the shock and the other subcluster and applied Method A to the data. Due to the limited coverage of the SIS in the outer areas, we used only the GIS data. A region 5' in diameter centered on NGC 3862 was once again excluded from the analysis.

The summed spectra for each region were fit with a Raymond-Smith model to determine the temperatures. For the SE subcluster annular regions we find temperatures from Method A for the GIS data only of  $3.1 \pm 0.1$  keV,  $3.1 \pm 0.2$  keV and  $3.6 \pm 0.4$  keV for the inner, intermediate and outer annuli respectively. For the NW subcluster the Method A GIS only temperatures were  $4.9 \pm 0.5$  keV,  $4.7 \pm 0.4$  keV and  $4.6 \pm 0.7$  keV for the inner, intermediate and outer annuli respectively. We note that the large errors in the outermost annuli are due to their close proximity to the edge of the GIS imaging area. Both profiles are consistent with isothermal conditions and with the previous measured temperatures from the appropriate rectangular regions.

We know from our previous results that there is temperature structure in the cluster, namely the shock. However, to derive an estimate of the masses, we assume isothermality throughout each subcluster. We used the weighted average temperatures ( $T_c$ ) of 3.2 keV and 4.2 keV applied to Equation 2 to calculate the mass within 0.5 Mpc. These include the results from both Method A and Method B for the GIS and SIS detectors. We also have extrapolated the observed mass to that within 1 Mpc for ease of comparison with previous work. The temperature of 4.2 keV—instead

of those listed above— was selected for the NW subcluster due to the consistently higher results found for it (regions #6, #7 and #8) using Method A with the GIS data (see Figure 4). The resultant mass estimates are given in Table 2.

The second hydrostatic equilibrium mass estimate uses the same gas density profile as the first, but with a different temperature. We have used the empirical relation between temperature and luminosity from David et al. (1993),

$$kT_{eff} = 10^{-0.72} \left( \frac{L_{bol}}{10^{40}} \right)^{0.297} \quad (3)$$

to estimate an effective temperature ( $T_{eff}$ ) for a similarly luminous, but undisturbed, cluster.

We determined the total flux within the ROSAT band— from 0.5 to 2.0 keV— from each of the previously defined annuli. Applying azimuthal symmetry, we found the total flux within a radius of 18' (0.66 Mpc) for each subcluster, and then calculated the bolometric luminosity (David et al. 1997).

Finally, the gas mass was estimated by inverting the formula from David et al. (1990),

$$L(r) = \frac{2\pi n_e n_H \Lambda_0 a^3}{(1 - 3\beta)} \times \int_0^{\infty} \left\{ \left[ 1 + s^2 + \left( \frac{r}{a} \right)^2 \right]^{-3\beta+1} - (1 + s^2)^{-3\beta+1} \right\} ds \quad (4)$$

and solving for the central density. We then integrated the density distribution to find the gas mass,

$$M_{gas} = 4\pi \rho_o \int_0^r r^2 \left( 1 + \left[ \frac{s}{R_c} \right]^2 \right)^{-\frac{3\beta}{2}} ds, \quad (5)$$

using the density distribution corresponding to the surface brightness given in Equation 1 for an isothermal gas with  $\rho_o = \mu_e n_e m_p$  where  $\mu_e$  is the mean molecular weight per electron.

The resultant gas masses are given in Table 2 and yield, when compared to the mass estimates (using  $T_{eff}$  for the NW subcluster), gas mass fractions of  $\sim 12\%$  at 0.5 Mpc and  $\sim 16\%$  at 1 Mpc in each subcluster which is typical of rich clusters.

Although, as stated above, there is considerable dispersion in the  $L_x - T$  relation, temperature estimates from the luminosity for both subclusters are lower than the measured values. For the SE subcluster the difference is moderate with an estimated temperature— and thus mass— 31% lower than the actual measured values. However, for the

NW subcluster the difference is nearly twice as large. We measure a luminosity of  $0.29 \times 10^{44}$  ergs  $s^{-1}$  and thus estimate a gas temperature of 2.0 keV which is 52% lower than the measured value of 4.2 keV. Again the results for the masses within 0.5 Mpc and 1.0 Mpc are given in Table 2.

As discussed above the estimates of the masses of the two subclusters have considerable uncertainty associated with them due to the perturbations from the merger. However, the two subclusters appear to be experiencing similar changes to their density profiles, thus allowing a *relative* comparison of their masses. While the masses derived from the measured temperatures are essentially equal, the NW subcluster appears to have been heated more than the SE subcluster, thus suggesting that it is actually less massive than the SE subcluster. This is further supported by the calculated gas mass.

#### 4. CONCLUSION

We have analyzed the ROSAT PSPC and ASCA SIS and GIS observations of A1367. For the ASCA data, we have applied two different analysis techniques for measuring the intracluster gas temperature and find excellent agreement.

Our analysis indicates that we are observing the early stages of a slightly unequal merger between the two subclusters occurring along a SE-NW axis nearly in the plane of the sky. We find evidence for a shock-like feature along the merger axis between the two subclusters as well as heating of the gas throughout both subclusters, with the smaller NW subcluster being heated more than the SE subcluster. This is in excellent agreement with predictions from the merger simulations by Evrard (1990a and b) and Schindler & Müller (1993). We also note that the surface brightness profile of the NW subcluster is “puffing out” as indicated by its larger core radius. This is similar to the effects identified by Roettiger et al. (1996) as a signature of a merger event.

Our detailed temperature map of the cluster suggests that the merger may be occurring slightly obliquely, with the cluster cores passing each other traveling north-south, but the statistics of the data are not sufficient to support any firm conclusion on this point.

Future studies of A1367 and other merging clusters will provide a clearer picture of the detailed interactions which occur as clusters form. With the launch of AXAF in 1998, we can expect to obtain much higher angular resolution temperature maps to study the merger process and the structure of the shocks which are produced.

RHD, MM, WF, CJ and LPD acknowledge support from the Smithsonian Institute and NASA contract NAS8-39073.

#### REFERENCES

Arnaud, K. 1993 *ASCA* Newsletter, No. 1 (NASA/GSFC)  
 Bahcall, N. 1977 *ARA&A*, 18, 505  
 Bechtold, J., Forman, W., Giacconi, R., Jones, C., Schwarz, J., Tucker, W., & Van Speybroeck, L. 1983, *ApJ*, 265, 26  
 Bird, C. M. 1994, *AJ*, 107, 1637  
 Cavaliere, A., & Fusco-Femiano, R. 1976, *A&A*, 49, 137  
 Churazov, E., Gilfanov, M., Forman, W., & Jones, C. 1996a, in *Proc. Röntgenstrahlung from the Universe*, eds. Zimmerman, H. U., Trümper, J., & Yorke, H., MPE Report 263, 573  
 Churazov, E., Gilfanov, M., Forman, W., & Jones, C. 1996b, *ApJ*, 471, 673  
 Churazov, E., Gilfanov, M., Forman, W., & Jones, C. 1997, *in preparation*  
 David, L. P., Arnaud, K.A., Forman, W., & Jones, C. 1990, *ApJ*, 356, 32  
 David, L. P., Slyz, A., Jones, C., Forman, W., Vrtilek, S.D., & Arnaud, K.A. 1993, *ApJ*, 412, 479  
 David, L. P., Jones, C., & Forman, W. 1997, *in preparation*  
 Dressler, A. & Shectman, S. A. 1988, *AJ*, 985

Edge, A.C. & Stewart, G.C. 1991, MNRAS, 252, 428

Evrard, A. E. 1990a, ApJ, 363, 349

Evrard, A. E. 1990b, in Clusters of Galaxies, eds. Oegerle, Fitchett and Danly (Cambridge: Cambridge University Press), 287

Evrard, A. E., Metzler, C. A., & Navarro, J. F. 1996, ApJ, 469, 494

Forman, W., Bechtold, J., Blair, W., Giacconi, R., Van Speybroeck, L., & Jones, C. 1981, ApJ, 243, L133

Forman, W. & Jones, C. 1982, ARA&A, 20, 547

Gavazzi, G., Contursi, A., Carrasco, L., Boselli, A., Kennicutt, R., Scodéglio, M., & Jaffe, W. 1995, A&A, 304, 325

Geller, M.J., & Beers, T.C. 1982, PASP, 94, 421

Gilfanov, M., Churazov, E., Forman, W., & Jones, C. 1997, in preparation

Grebenev, S.A., Forman, W., Jones, C., & Murray, S. 1995, ApJ, 445, 605

Jones, C. and Forman, W. 1992, in Clusters and Superclusters of Galaxies, ed. A.C. Fabian

Jones, C. & Forman, W. 1984, ApJ, 276, 38

Jones, C., & Forman, W. 1997, submitted

Markevitch, M., Mushotzky, R., Inoue, H., Yamashita, K., Furuzawa, A., & Tawara, Y. 1996, ApJ, 456, 437

Markevitch, M., Forman, W. R., Sarazin, C.L., & Vikhlinin, A. 1997, submitted

Mohr, J., Fabricant, D.G., Geller, M. J., and Evrard, A.E. 1994, BAAS, 185, #118.07

Roettiger, K., Burns, J.O., & Loken, C. 1996, ApJ, 473, 651

Schindler, S., & Müller, E. 1993, A&A, 272, 137

Slezak, E., Durret, F., & Gerbal, D. 1994, AJ, 108, 1996

Snowden, S.L. 1994, Cookbook for Analysis Procedures for ROSAT XRT/PSPC Observations of Extended Objects and the Diffuse Background

Snowden, S. L., McCammon, D., Burrows, D. N., & Mendenhall, J. A. 1994, ApJ, 424, 714

Takahashi, T., Markevitch, M., Fukazawa, Y., Ikebe, Y., Ishisaki, Y., Kikuchi, K., Makishimi, K., & Tawara, Y. 1995, *ASCA* Newsletter, No. 3 (NASA/GSFC)

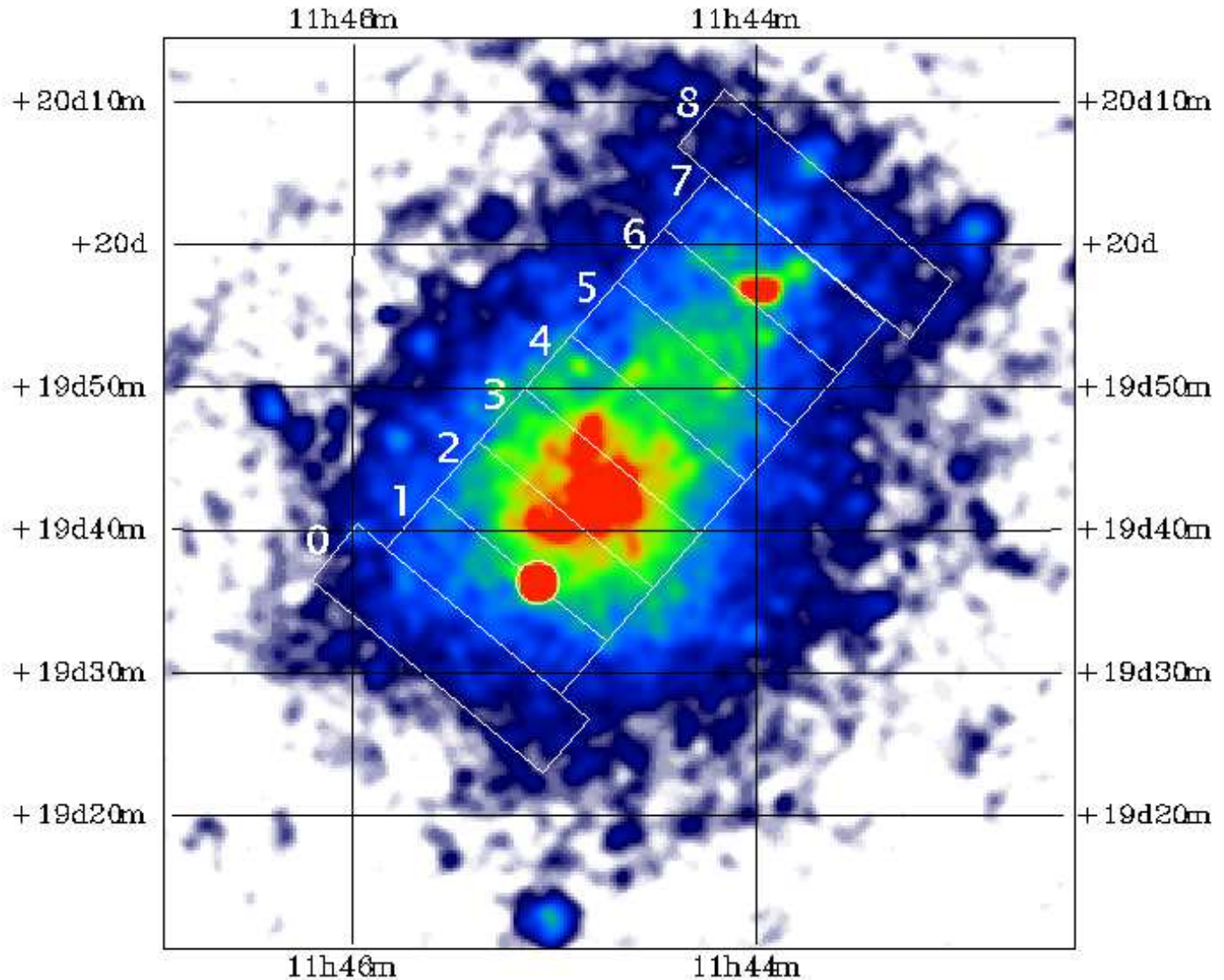


FIG. 1.— Central  $1^\circ \times 1^\circ$  of the PSPC image of A1367 with no background subtraction. This scale was chosen to allow easy comparison with the ASCA data. The outline of the regions used in the spectral fitting for both methods are shown. Also shown is the excluded circular region surrounding NGC 3862.

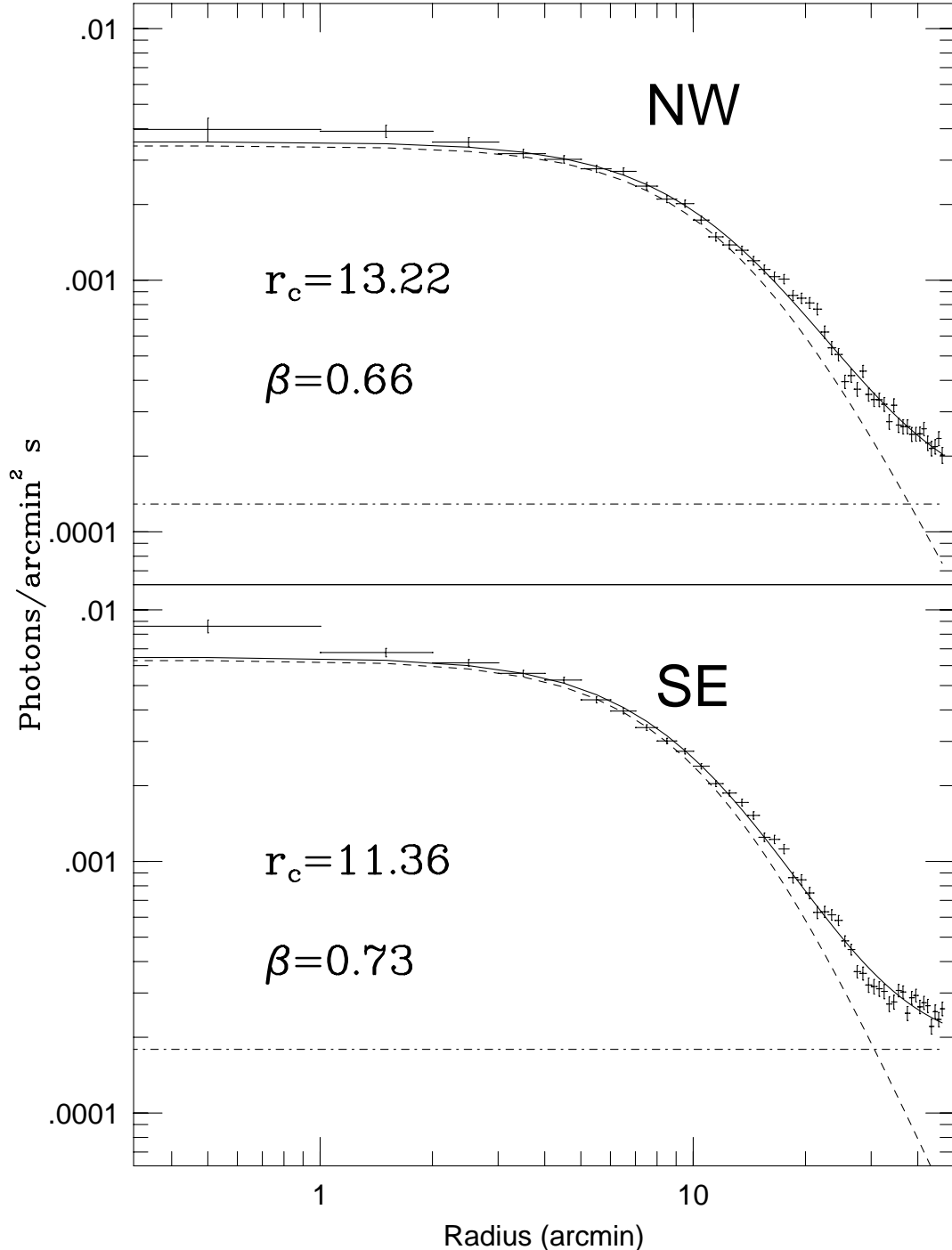


FIG. 2.—  $\beta$ -model fits (dashed lines) with constant backgrounds (dash-dotted lines) for the two subclusters. Core radii are given in arcminutes and are 0.49 and 0.42 Mpc for the NW and SE subclusters respectively.

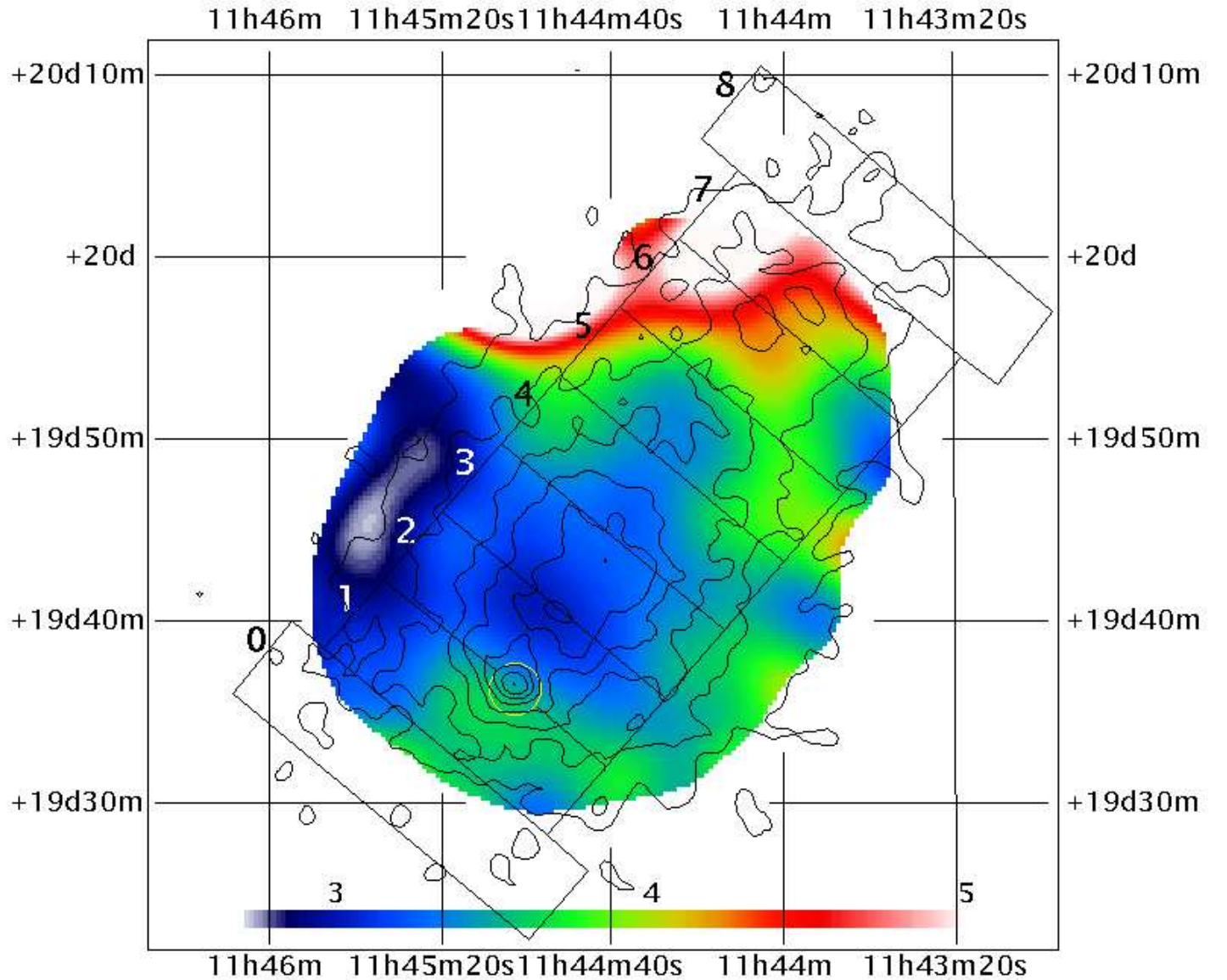


FIG. 3.— Smoothed continuous temperature map from ASCA GIS data of the A1367. The regions used later in the fitting process and shown previously in Figure 1 are again outlined as is the excluded circular region around NGC 3862. Pixels with large uncertainties in their temperatures ( $\frac{T+\sigma_T}{T-\sigma_T} > 1.5$ ) have been excluded from this map. The SIS data does not extend beyond regions #1 and #7 and the GIS results for regions #0 and #8 displayed in Table 3 and Figure 4 are shown for completeness. A scale bar for the temperature is provided for ease of reference.

### ASCA Temperature Profile for A1367

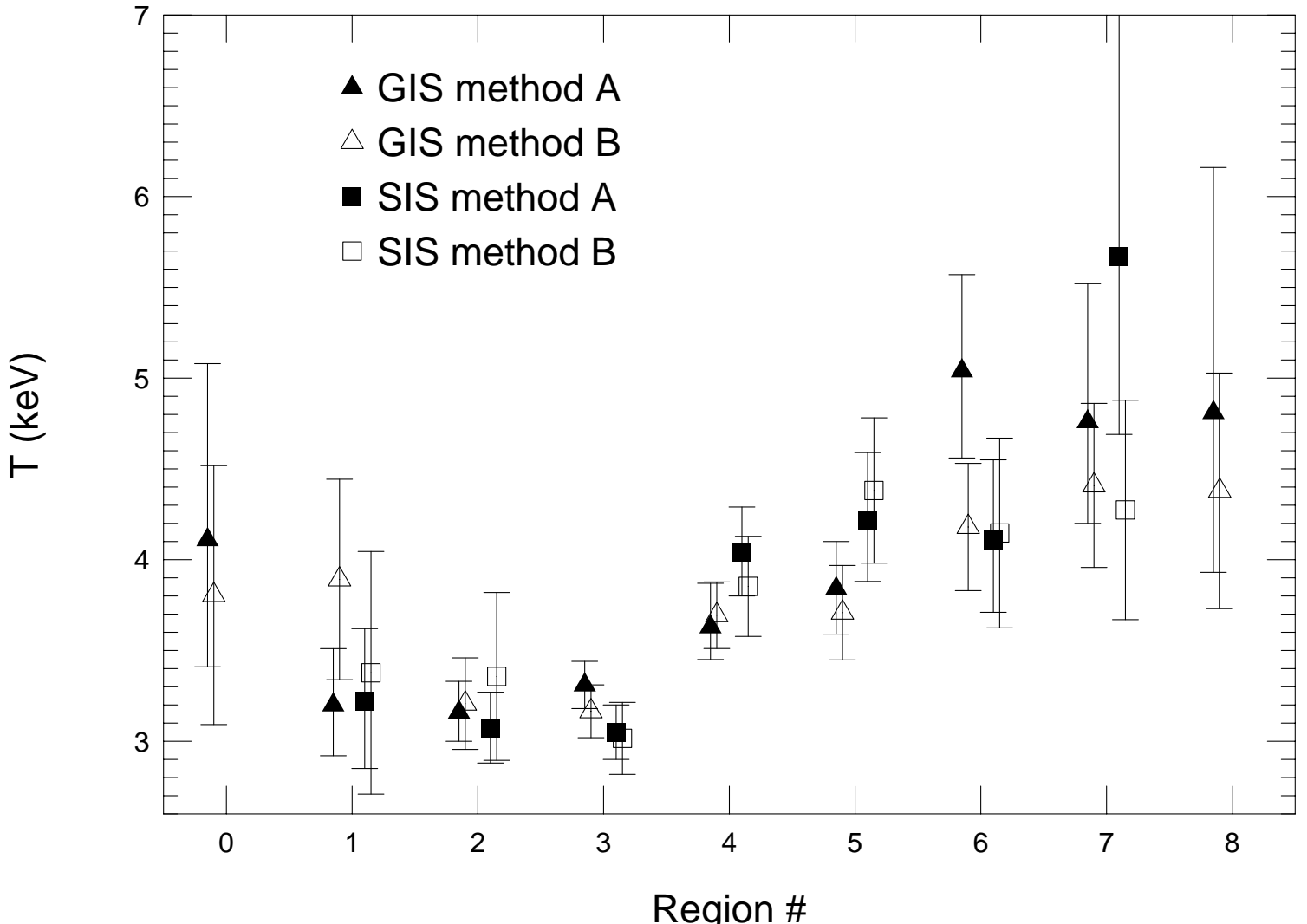


FIG. 4.— Fitted temperatures from the two methods with their respective  $1\sigma$  error bars. Regions #1 through #7 were 5' wide and 16' long with the short axis aligned to a line running between the SE and NW subclusters. Region #0 and #8 were 5' wide and 21' long with the same orientation (see Figure 1 or Figure 3). Note the excellent agreement between all of the various results, with the one exception being for the GIS data in region #6 with Method A. The large error bar for the SIS data in region #7 is due to the edge of the data. Also GIS results for regions #0 and #8 which both lie beyond the SIS frame area are included for completeness.

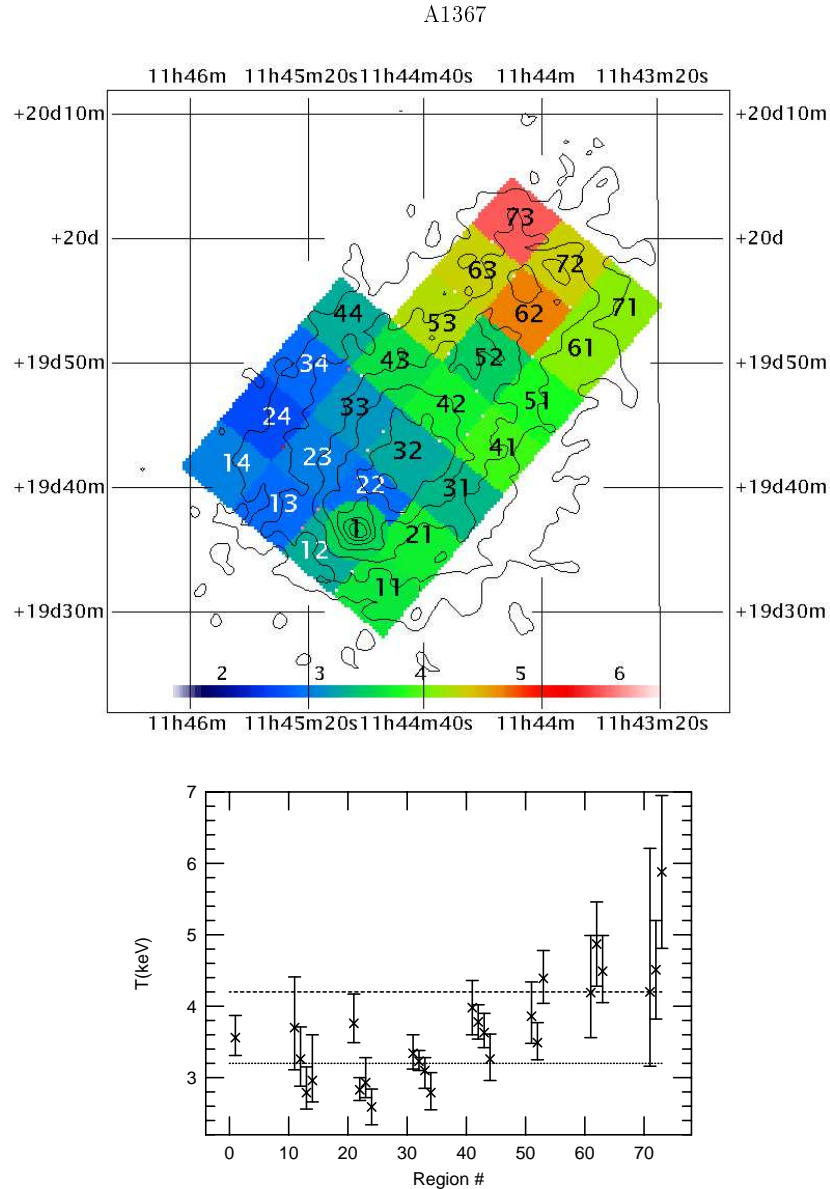


FIG. 5.— Two dimensional temperature map of A1367. The subregions were constructed by dividing the previously defined rectangles into three equal parts. Note the numbering scheme was chosen to highlight the association with the previous results. Also included were four new regions—#14, #24, #34, and #44— that encompass the cool area to the northeast. The temperatures were determined by simultaneously fitting the GIS and SIS data. The peaks of the emission for the SE and NW subclusters are approximately located in subregions #32 and #62 respectively. The statistics of all other areas either precluded subdivision—e.g. regions #0 and #8— or simply produced no meaningful results even when not subdivided. Again a scale bar for the temperature is provided. Included below the map, for ease of comparison, is a plot of the temperatures versus region number with  $1\sigma$  errorbars. We have drawn lines at 3.2 and 4.2 keV to indicate the weighted averages for the two subclusters.

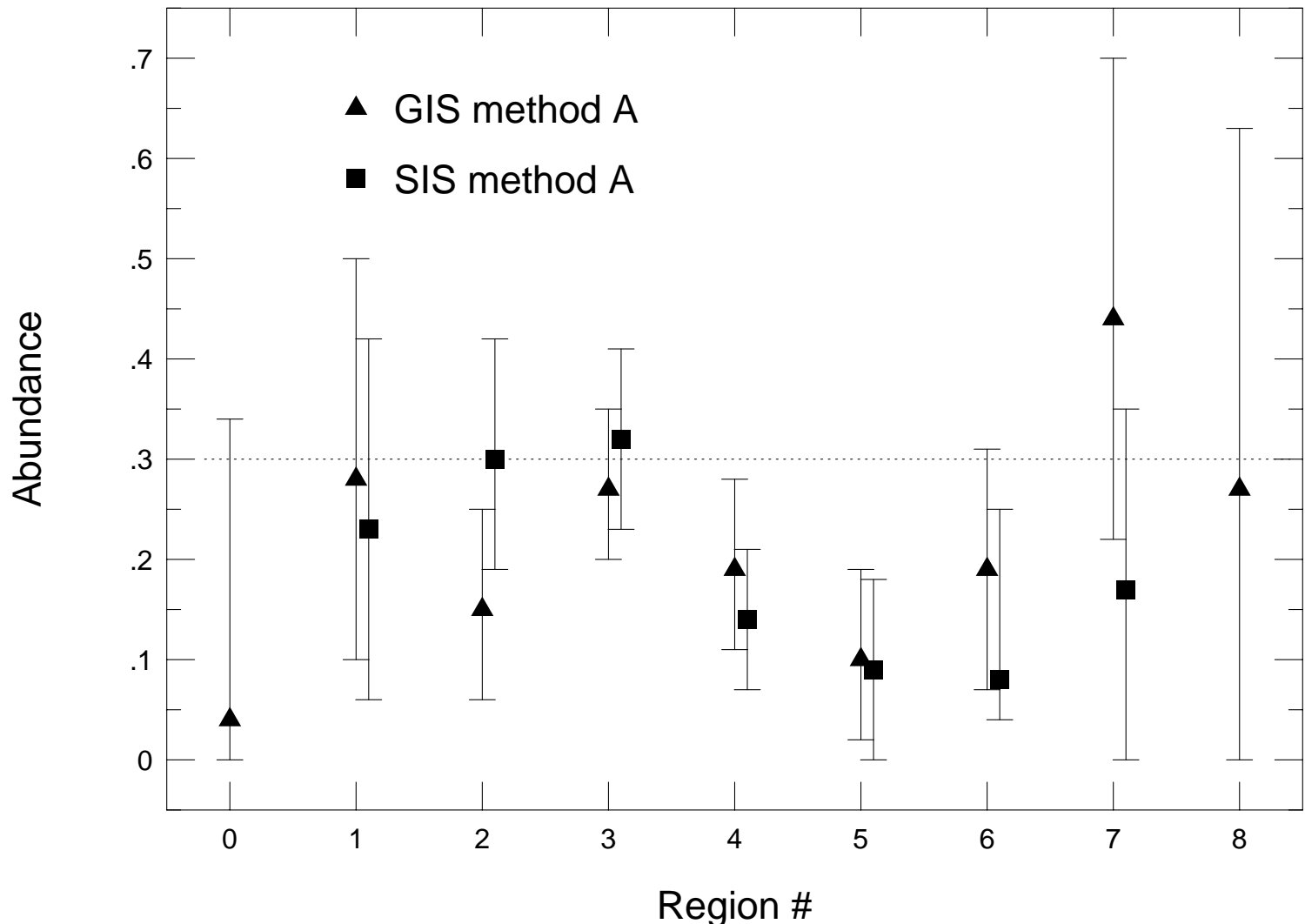


FIG. 6.—Fitted abundances from Method A with their respective  $1\sigma$  error bars. Also shown is the abundance used for the results for Method B and the continuous map generated from Method A (Figure 3). We note that changing the abundance to 0.4 for Method B had no significant effect on the fitted temperatures.

TABLE 1  
OBSERVATIONAL DATA

Pointing	$\alpha^a$	$\delta^a$	On/Live Time <sup>b</sup>			Events			
			GIS-2/3 <sup>c</sup>	SIS-0	SIS-1	GIS-2	GIS-3	SIS-0	SIS-1
ASCA-SE1	$11^h44^m52.8^s$	$19^{\circ}41'45.6''$	7,292	6,462	4,481	8,482	8,236	11,248	8,053
ASCA-SE2	$11^h44^m57.6^s$	$19^{\circ}43'19.2''$	9,654	7,452	6,710	11,108	10,881	13,121	11,629
ASCA-NW1	$11^h44^m26.4^s$	$19^{\circ}51'57.6''$	10,624	6,944	5,888	11,683	11,664	10,820	9,351
ASCA-NW2	$11^h44^m31.2^s$	$19^{\circ}50'24.0''$	8,030	6,490	4,606	9,077	8,996	10,081	7,561
ROSAT-PSPC	$11^h44^m40.8^s$	$19^{\circ}42'36.0''$		16,357				203,890	

<sup>a</sup>J2000

<sup>b</sup>Units of seconds.

<sup>c</sup>On-Time for the GIS-2 and GIS-3 detectors were the same.

TABLE 2  
SUBCLUSTER DATA

Subcluster	$\beta$	$R_c^a$	$T_c^b$	$M_{total}^c$		$L_{0.66\text{Mpc}}^d$	$M_{gas}^c$		$T_{eff}^b$	$M'_{total}^c$	
				$0.5^a$	$1.0^a$		$0.5^a$	$1.0^a$		$0.5^a$	$1.0^a$
SE	$0.73 \pm 0.03$	$0.42 \pm 0.02$	3.2	0.77	2.3	0.39	0.061	0.22	2.2	0.53	1.5
NW	$0.66 \pm 0.05$	$0.49 \pm 0.04$	4.2	0.78	2.5	0.29	0.049	0.20	2.0	0.38	1.2

<sup>a</sup>Mpc

<sup>b</sup>keV

<sup>c</sup>Masses given are within the radius listed and in units of  $\times 10^{14} M_{\odot}$

<sup>d</sup> $\times 10^{44}$ ergs s<sup>-1</sup>

TABLE 3  
RESULTS OF SPECTRAL FITS IN THE REGIONS

	0	1	2	3	4	5	6	7	8
Temperatures <sup>a</sup>									
GIS-A	$4.1_{-0.7}^{+1.0}$	$3.2 \pm 0.3$	$3.2 \pm 0.2$	$3.3 \pm 0.1$	$3.6 \pm 0.2$	$3.8 \pm 0.3$	$5.0 \pm 0.5$	$4.8_{-0.6}^{+0.8}$	$4.8_{-0.9}^{+1.4}$
GIS-B	$3.8 \pm 0.7$	$3.9 \pm 0.6$	$3.2 \pm 0.3$	$3.2 \pm 0.1$	$3.7 \pm 0.2$	$3.7 \pm 0.3$	$4.2 \pm 0.4$	$4.4 \pm 0.5$	$4.4 \pm 0.6$
SIS-A	...	$3.2 \pm 0.4$	$3.1 \pm 0.2$	$3.1 \pm 0.2$	$4.0_{-0.2}^{+0.3}$	$4.2_{-0.3}^{+0.4}$	$4.1 \pm 0.4$	$5.7_{-1.0}^{+1.6}$	...
SIS-B	...	$3.4 \pm 0.7$	$3.4 \pm 0.5$	$3.0 \pm 0.2$	$3.9 \pm 0.3$	$4.4 \pm 0.4$	$4.1 \pm 0.5$	$4.3 \pm 0.6$	...
Abundances <sup>b</sup>									
GIS-A	$0.04_{-0.04}^{+0.30}$	$0.28_{-0.18}^{+0.22}$	$0.15_{-0.09}^{+0.10}$	$0.27_{-0.07}^{+0.08}$	$0.19_{-0.08}^{+0.09}$	$0.10_{-0.08}^{+0.09}$	$0.19_{-0.12}^{+0.12}$	$0.44_{-0.22}^{+0.26}$	$0.27_{-0.27}^{+0.36}$
SIS-A	...	$0.23_{-0.17}^{+0.19}$	$0.30_{-0.11}^{+0.12}$	$0.32_{-0.09}^{+0.09}$	$0.14_{-0.07}^{+0.07}$	$0.09_{-0.09}^{+0.09}$	$0.08_{-0.04}^{+0.17}$	$0.17_{-0.17}^{+0.18}$	...

<sup>a</sup>Temperatures are in keV. The errors quoted are  $1\sigma$ .

<sup>b</sup>Abundances are relative to solar with  $\frac{N_{Fe}}{N_{Total}} = 4.68 \times 10^{-5}$  assumed. The errors quoted are  $1\sigma$ .